

Supplementary Materials

All-solid-state proton batteries with a wide operation-temperature range of 160 °C

**Lifen Long¹, Yike Huang¹, Yun Zheng¹, Yan Guo¹, Yinan Liu¹, Yingying Shen¹,
Pingshan Jia¹, Zikang Xu¹, Shengyang Dong^{1,2,*}, Huaiyu Shao^{1,*}**

¹Institute of Applied Physics and Materials Engineering, University of Macau, Macau 999078, China.

²Jiangsu Key Laboratory of New Energy Devices & Interface Science, School of Chemistry and Materials Science, Nanjing University of Information Science and Technology, Nanjing 210044, Jiangsu, China.

***Correspondence to:** Prof. Huaiyu Shao, Institute of Applied Physics and Materials Engineering, University of Macau, Macau 999078, China. E-mail: hshao@um.edu.mo; Prof. Shengyang Dong, Jiangsu Key Laboratory of New Energy Devices & Interface Science, School of Chemistry and Materials Science, Nanjing University of Information Science and Technology, Nanjing 210044, Jiangsu, China. E-mail: dongsys@nuist.edu.cn

ORCID: Huaiyu Shao (0000-0001-9286-7071)

Notes:

Supplementary Video 1: Bubbles were produced when the Al foil was placed in 1 M H_3PO_4 .mp4

Supplementary Video 2: No bubbles are produced when the Al foil is placed with ZHP.mp4

Supplementary Video 3: No bubbles were produced when the electrodes MoO_3 and H-TBA were placed with ZHP.mp4

Note1:

The impedance used in conductivity calculation was the interception of the impedance curve of ZHP with the Z' axis. The ionic conductivity, in $S\ cm^{-1}$, was calculated from the Equation (1), where σ is the sample ionic conductivity, l is the electrolyte thickness, and the S is the electrolyte area in contact with the electrode.

$$\sigma = \frac{l}{RS} \quad (1)$$

The Arrhenius activation energy (E_a) was calculated from the Equation (2), where R is the ideal gas constant, A is the pre-exponential facto and T is the temperature.

$$\sigma = Ae^{-\frac{E_a}{RT}} \quad (2)$$

Note 2:

Full cell parameters: The electrode mass loading, N/P ratio, areal capacity, and estimated energy density in the revised Supplementary Information. The mass of the H-TBA cathode active material was approximately 1.5 mg with an electrode diameter of 10 mm, corresponding to a mass loading of approximately $1.27\ mg\ cm^{-2}$. The N/P ratio was close to 2:1. At $10\ mA\ g^{-1}$, the full cell delivered a specific capacity of $44\ mAh\ g^{-1}$, corresponding to an areal capacity of approximately $0.056\ mAh\ cm^{-2}$. An average discharge voltage of 0.45 V was used to estimate the energy density, giving an energy density of approximately $19.8\ Wh\ kg^{-1}$ based on the cathode active material.

Supplementary Table 1. ICP-OES results for initial ZHP.

Element	Zr	P
Weight	24.9%	27.3%
Molar ratio	1	3.2

Supplementary Table 2. Structural parameters and fitting quality statistics were obtained by refinement of structural models from the XRD pattern of ZHP.

Chemical formula	ZrH _{5.4} P _{3.2} O _{12.7}	
Crystal system	Trigonal	
Space group	R-3c (NO.167)	
Unite cell parameter		
a	8.25738	
b	8.25738	
c	25.6243	
V	1513.099	
Atomic parameter		
Zr 6b (0,0,0)	U _{iso}	0.0201
P1 18e (x,0,1/4)	x	0.66807
	U _{iso}	0.04332
O1 36f (x, y, z)	x	0.50685
	y	0.90404
	z	0.21476
	U _{iso}	0.039
O2 36f (x, y, z)	x	0.72234
	y	0.86999
	z	0.28674
	U _{iso}	0.05699
Statistics		
GOF	3.63	
Rwp	6.17%	
Rp	4.37%	

Supplementary Table 3. Bond lengths and angles were obtained from the crystal structure of ZHP.

Bond length (Å)	
Zr-O1	2.14596
P1-O1	1.46992
P1-O2	1.64945
O2···O2	2.64626
O2-H1 ^{a)}	1.11279
O2-H2 ^{a)}	1.12539
Bond angle (°)	
O1-Zr1-O1	90.3049
	180
	89.6951
O1-P1-O1	100.9915
O1-P1-O2	117.8612
	106.9986
O2-P1-O2	106.6742

^{a)} Obtained from the BVSE calculations.

Note: The formation of hydrogen bonds is closely related to the distance between the proton and the acceptor oxygen atom, the distance between the donor and acceptor oxygen atoms, and the O-H···O bond angle.^[1] According to XRD refinement and BVSE calculations (Table S3), the proton acceptor O distance is significantly shorter than the sum of van der Waals radii yet longer than a covalent bond; the O···O distance is less than 3 Å; and the O-H···O bond angle ranges from 170° to 180°, approaching linearity. These results indicate that the chemical environment within ZHP is favorable for hydrogen bond formation.

Supplementary Table 4. Comparison of different electrolytes and this study at different temperatures.

Material	Proton conductivity from -82 to -20 °C (mS cm ⁻¹)	Proton conductivity at room temperature (mS cm ⁻¹)	Proton conductivity from 100 to 150 °C (mS cm ⁻¹)	Ref.
2 M H ₂ SO ₄ + 2 M MnSO ₄	22.3 (-40 °C)	139.9	-	[2]
PolyAS-EG ₄₅ hydrogel	1.51 (-50 °C)	-	-	[3]
HUP-3	5.84 × 10 ⁻⁴ (-40 °C)	3.62	-	[4]
PA@PNDI-COF at ambient humidity	4.2 (-30 °C)	18.8	-	[5]
PPM-12 hydrogel	3.47 (-20 °C)	7.56	-	[6]
AiCEs	0.023 (-82 °C)	15	-	[7]
SSAE (quasi-solid-state electrolyte)	1.5 (-70 °C)	95	-	[8]
H ₃ PO ₄ /MeCN	-	0.5	-	[9]
Nafion™ 212 at 95% RH	-	42	-	[10]
H ₅ SiMo ₁₁ VO ₄₀ ·8H ₂ O at 70% RH	-	5.7	-	[11]
MSA@ZIF-8-C-64%	-	16.2	64.8 (100 °C)	[12]
ZrH ₅ (PO ₄) ₃	-	5	31 (110 °C)	[13]
MeSA@PBI-COF	-	19.5	115 (130 °C)	[14]
MeSA@sCOF	-	28.7	58.9 (100 °C)	[15]
MeSA@H ₂ PPc	-	8.25	72 (110 °C)	[16]
[Zn ₃ (H ₂ PO ₄) ₆ (H ₂ O) ₃] (BTA)	-	0.33	8 (120 °C)	[17]
This work	0.15 (-40 °C)	7.04	60 (110 °C)	-

Supplementary Table 5. Comparison of electrochemical performance of all-solid-state proton batteries.

Battery system	Current density (mA g ⁻¹)	Cycle number	Capacity retention (%)	Ref.
H-TBA/ AiCE /MoO ₃	1000	20000	74	[7]
CuFe-TBA/ Zn ₃ (H ₂ PO ₄) ₆ (H ₂ O) ₃ (BTA) /MoO ₃	10	-	-	[17]
Ni-PBA/MSA@ZIF-8-C/MoO ₃	100	100	64.7	[12]
Ni-PBA/MeSA@PBI-COF/MoO ₃	1000	8000	74.2	[14]
H-TBA/ZHP /MoO ₃	1000	12000	92	This work

Supplementary Table 6. Performance comparison between full cells with ZHP electrolyte and aqueous H₃PO₄ electrolyte.

System	Electrolyte	Capacity	Cycle number	Capacity retention	Ref.
H-VHCF//MoO ₃ /MXene	8.5 M H ₃ PO ₄	73.5 mAh g ⁻¹	6000	90%	[18]
CuFe-TBA//MoO ₃	1M H ₃ PO ₄	48 mAh g ⁻¹	100	~ 20%	[9]
H-TBA//MoO ₃	9.5 M H ₃ PO ₄	46 mAh g ⁻¹	1000	~85%	[19]
VHCF//h-WO ₃	9.5 M H ₃ PO ₄	67.78 mAh g ⁻¹	1000	100%	[20]
H-TBA//MoO ₃	ZHP	44 mAh g ⁻¹	12000	92%	This work

Supplementary Table 7. ICP results for ZHP proton electrolyte and liquid electrolyte after being used.

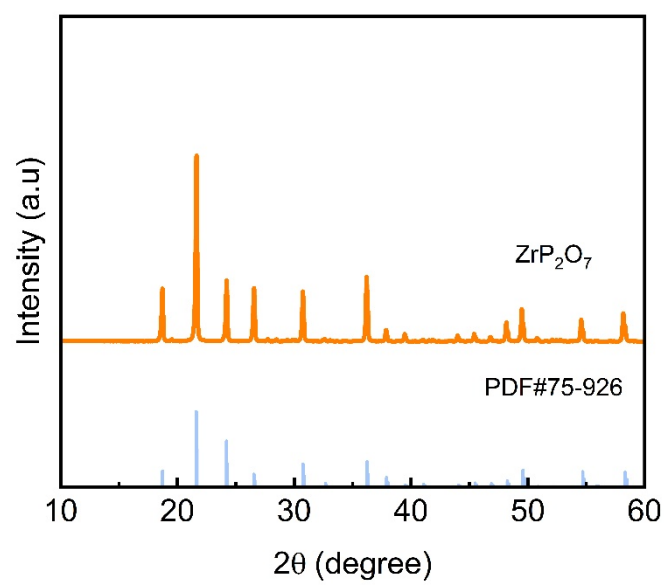
System	Cu	Fe	Mo	Ti	Al
After 12000 cycles (H-TBA/ZHP/MoO ₃)	0	0.04%	0	0.12%	–
After 10 days (Al/ZHP/Al)	–	–	–	–	0.18%
After 1000 cycles (H-TBA/Liquid H ₃ PO ₄ /MoO ₃)	5.7%	0.57%	33.01%	0.04%	–
Al in 1 M H ₃ PO ₄	–	–	–	–	3%

Note: “Al in 1 M H₃PO₄” refers to the aluminium content measured in the phosphoric acid after the sample was immersed in the 1 M H₃PO₄ solution for 24 hours.

Supplementary figures



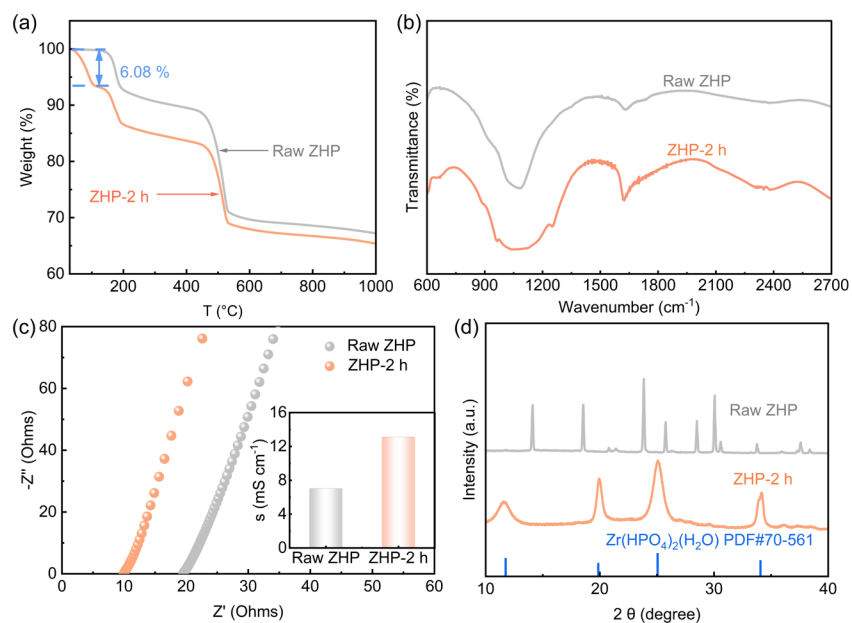
Supplementary Figure 1. Optical photograph of ZHP powder.



Supplementary Figure 2. The XRD curves of the TGA residue of ZHP.



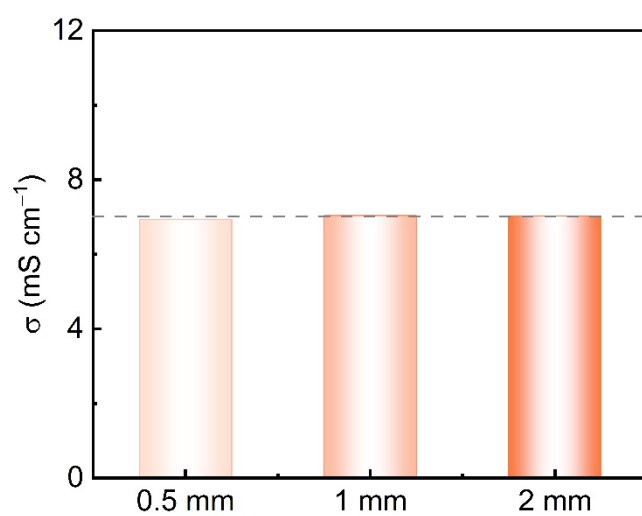
Supplementary Figure 3. The ZHP pellet is approximately ~1 mm thick and 10 mm in diameter by pressing ~200 mg of the powder of ZHP at 407 MPa.



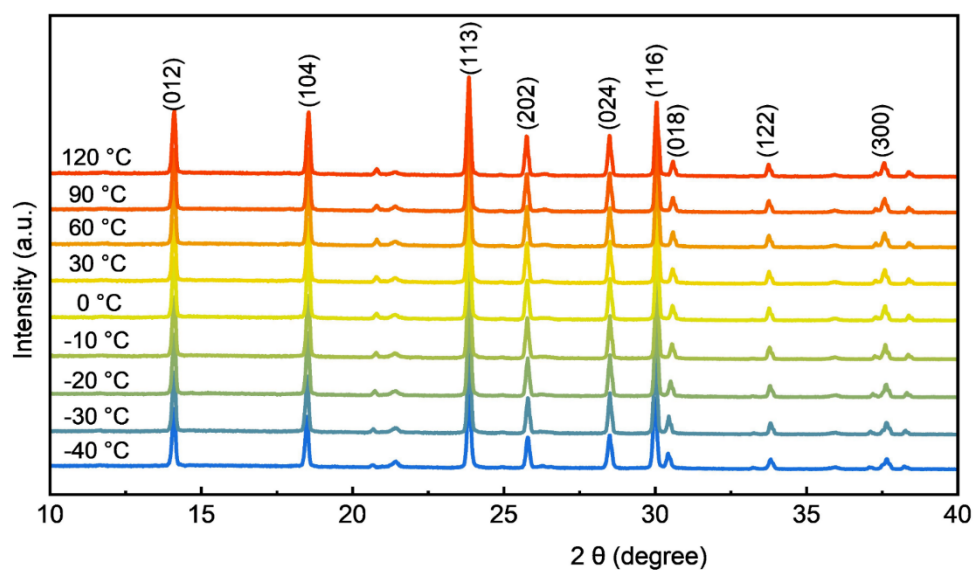
Supplementary Figure 4. (a) TGA curves of raw ZHP and ZHP-2 h. (b) FT-IR curves of raw ZHP and ZHP-2 h. (c) Nyquist plots of raw ZHP and ZHP-2 h. The inset diagram shows the ionic conductivity of ZHP raw ZHP and ZHP-2 h. (d) XRD patterns for raw ZHP and ZHP-2 h.

Note: the Nyquist plot measurements and all-solid-state battery tests were performed using coin cells under ambient laboratory conditions. However, all processes involving ZHP storage and coin-cell assembly were conducted under dry conditions ($\text{RH} \ll 1\%$) in an Ar-filled glovebox. Therefore, the “low humidity environment ($\text{RH} \ll 1\%$)” described in the manuscript mainly refers to the internal environment of the assembled cells, with the purpose of minimizing the influence of environmental moisture.

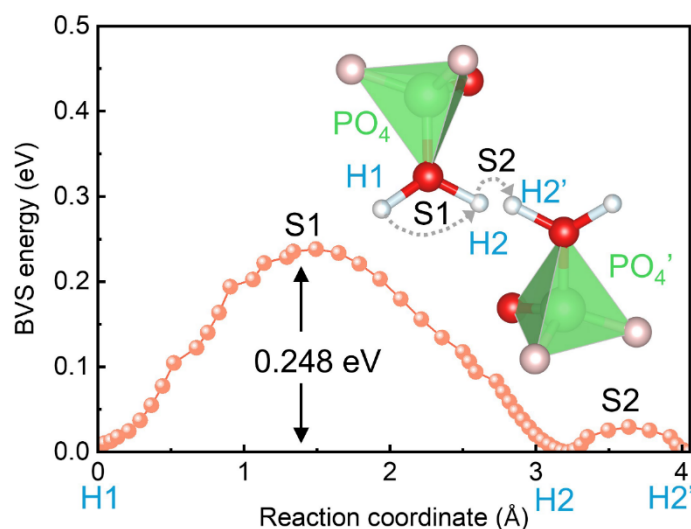
As shown in Figure R3, ZHP-2 h adsorbed approximately 6.08% moisture, accompanied by changes in the FT-IR signals and an obvious phase transition in the XRD pattern. Although the ionic conductivity increased after moisture adsorption, this increased conductivity is dependent on the adsorbed water/phase transformed structure. Therefore, the use of $\text{RH} \ll 1\%$ is not because ZHP cannot conduct under humid air, but rather to demonstrate that high proton conductivity can be achieved without relying on external moisture.



Supplementary Figure 5. The ionic conductivity of ZHP electrolytes with different thicknesses at room temperature.

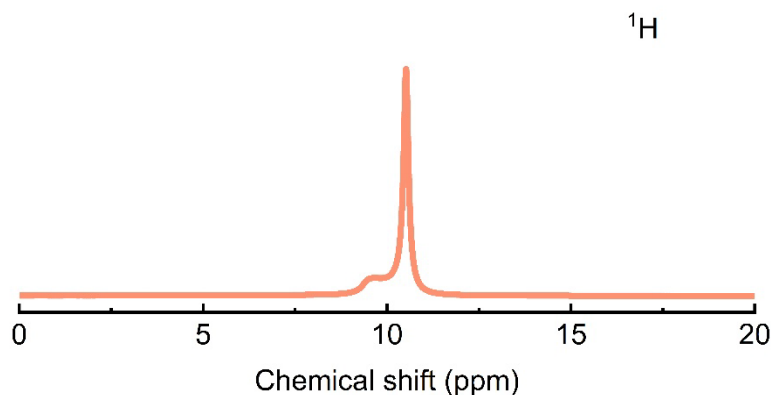


Supplementary Figure 6. Variable temperature X-ray diffraction data collected on heating the powder sample from -40 to 120 °C in 10 °C steps in vacuum. An equilibration time of 30 min was employed between -40 to 120 °C at each step.



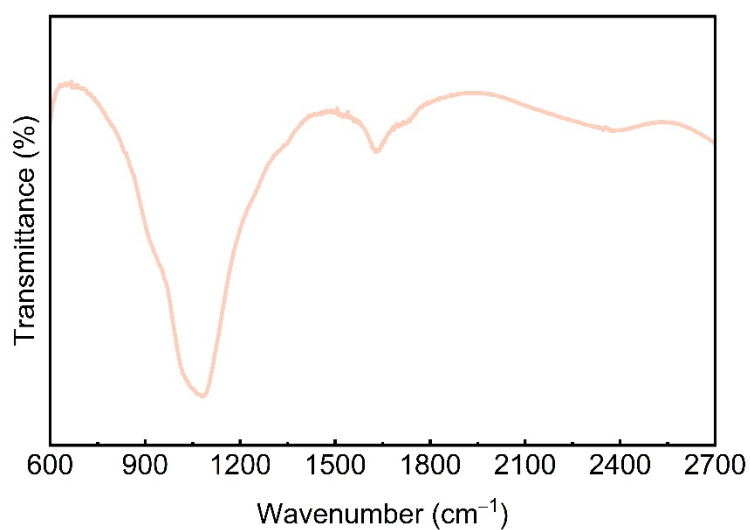
Supplementary Figure 7. Hydrogen ion migration barrier and schematic diagram of proton diffusion mechanism.

Notes: Proton migration adheres to a Grotthuss-like mechanism, involving a proton from position H1 around donor oxygen atoms rotating ($\sim 118.8^\circ$) to position H2 (or vice versa) and subsequently hopping onto a neighboring acceptor oxygen atom.^[13, 21] The activation energy for the rotation between the H1 and H2 on oxygen is 0.248 eV, which shows a close alignment with the activation energy determined through experiments. In contrast, the proton hopping that occurs between two neighboring oxygen atoms only requires a very small activation energy of 0.03 eV.



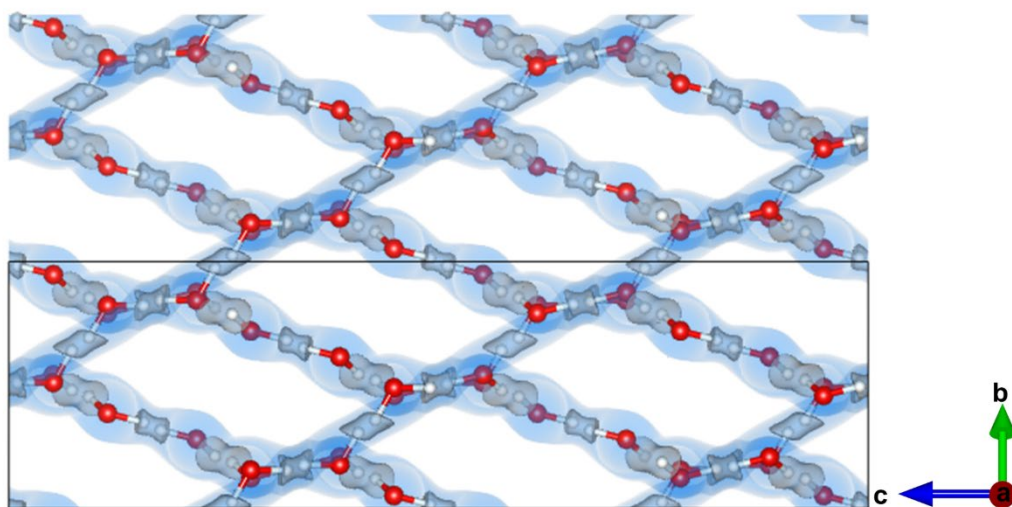
Supplementary Figure 8. ^1H SSNMR spectrum of ZHP.

Notes: In the monomeric forms of hypophosphorous acid and acetic acid, the -OH protons exhibit high-field ^1H SSNMR signals due to strong electronic shielding, typically appearing at 5.6~6.4 ppm and 4.5~5.5 ppm, respectively. Upon formation of intermolecular hydrogen bonds, the electron density around the -OH protons decrease, resulting in deshielding and a downfield shift of the resonance signals. For example, in the hypophosphorous acid-nitromethane complex and acetic acid dimers, the -OH proton signals shift to approximately 10~11 ppm due to strong hydrogen bonding. [22, 23] Similarly, the solid-state ^1H SSNMR spectrum of ZHP shows chemical shifts in the range of 9.2~11.3 ppm, indicating the presence of an internal hydrogen-bonding network.

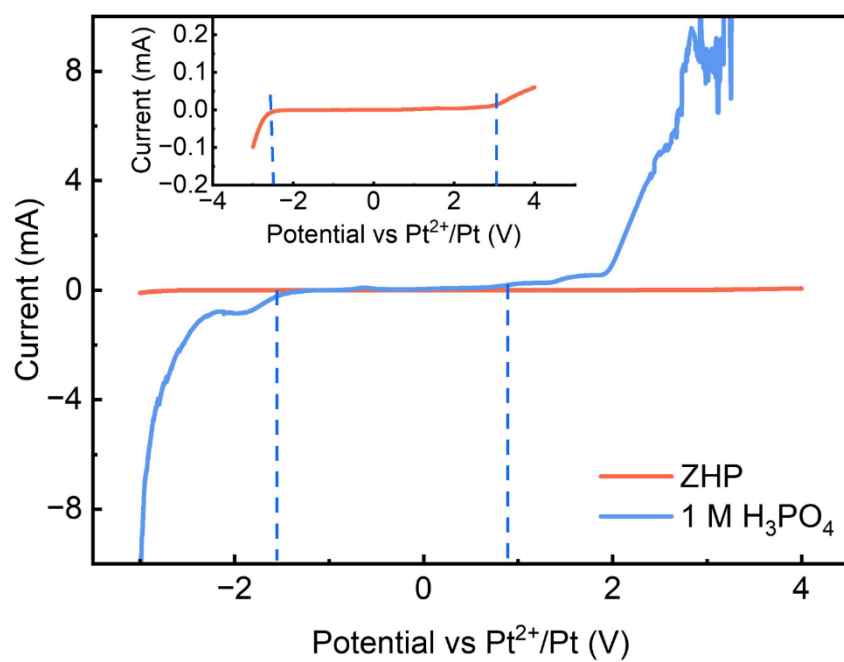


Supplementary Figure 9. FT-IR spectrum of raw ZHP.

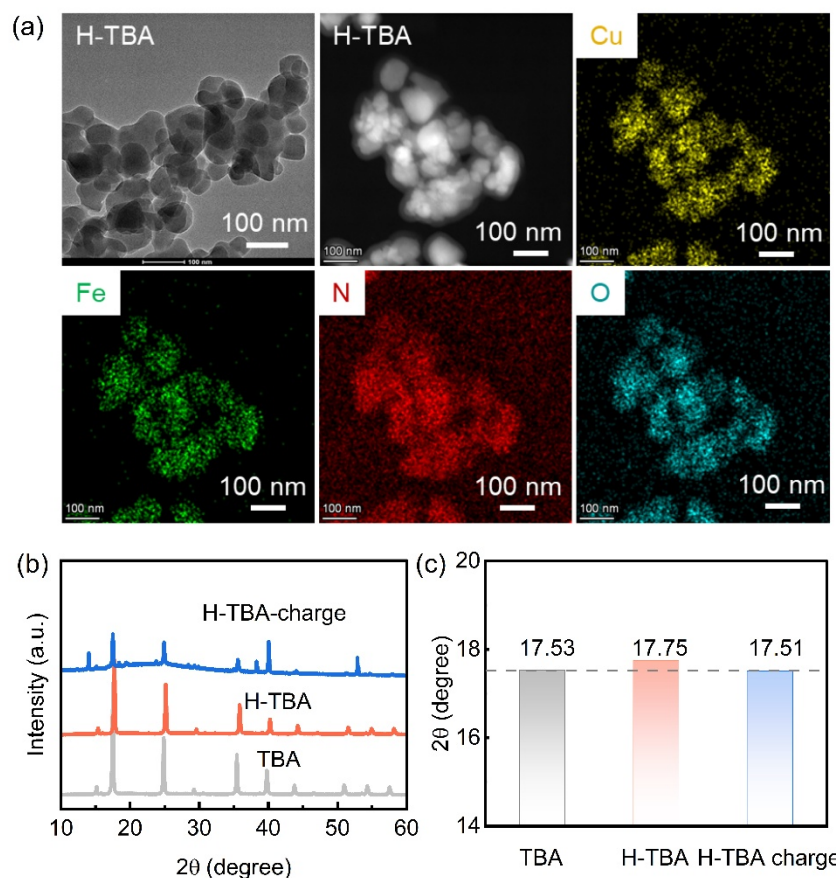
Notes: As shown in Figure S8, the spectrum of the powder sample in KBr medium displays an absorption band at 1079 cm^{-1} , attributed to the P-O stretching vibration. The broad bands at 1992 cm^{-1} and 2529 cm^{-1} are assigned to P-OH vibrations, this further confirms the formation of hydrogen bonds within the ZHP structure.^[24, 25]



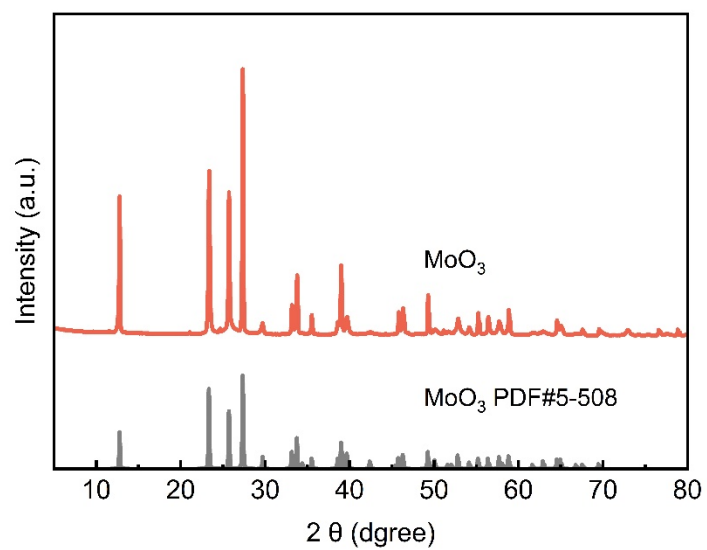
Supplementary Figure 10. Diagram of hydrogen bond network in ZHP without PO_4 and ZrO_6 .



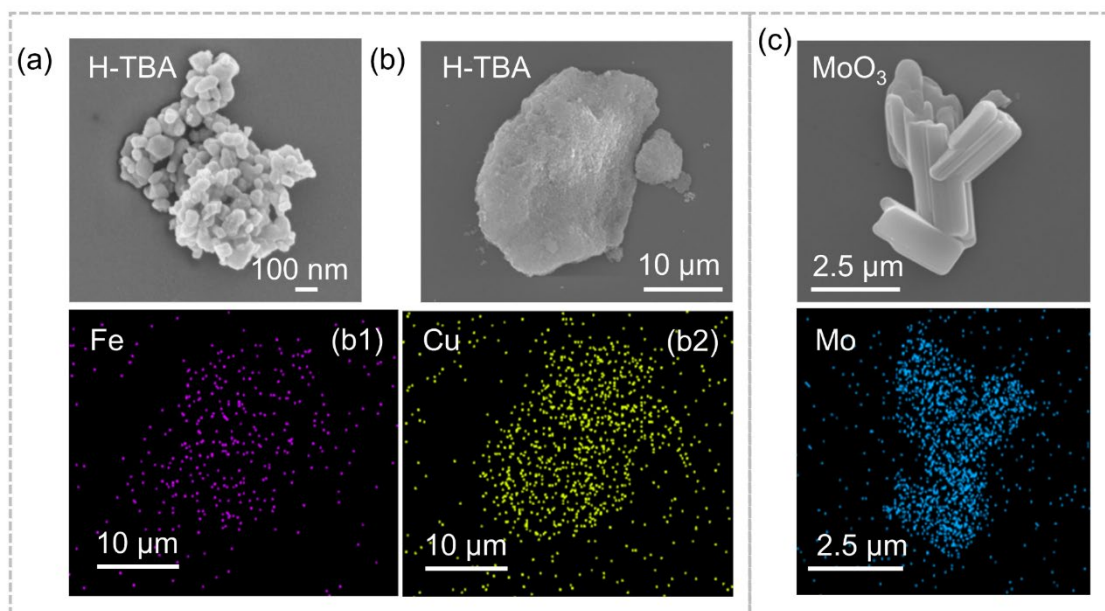
Supplementary Figure 11. LSV curves for electrolytes of ZHP and 1 M H₃PO₄.



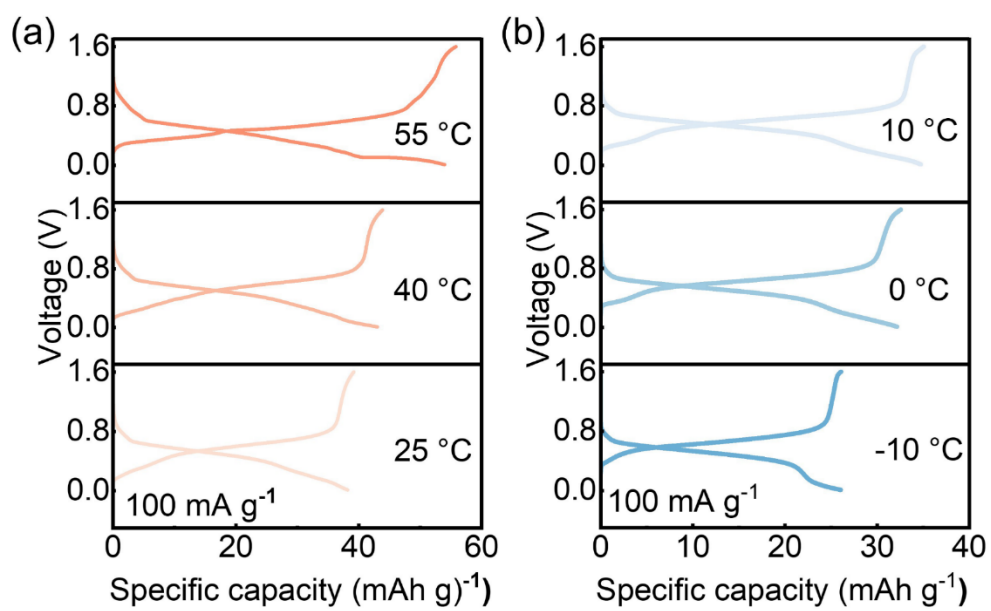
Supplementary Figure 12. a) TEM images of H-TBA and the corresponding elemental mapping. b) XRD patterns of H-TBA, TBA, and H-TBA-charged. c) Comparison of the XRD peak positions of H-TBA, TBA, and H-TBA-charged.



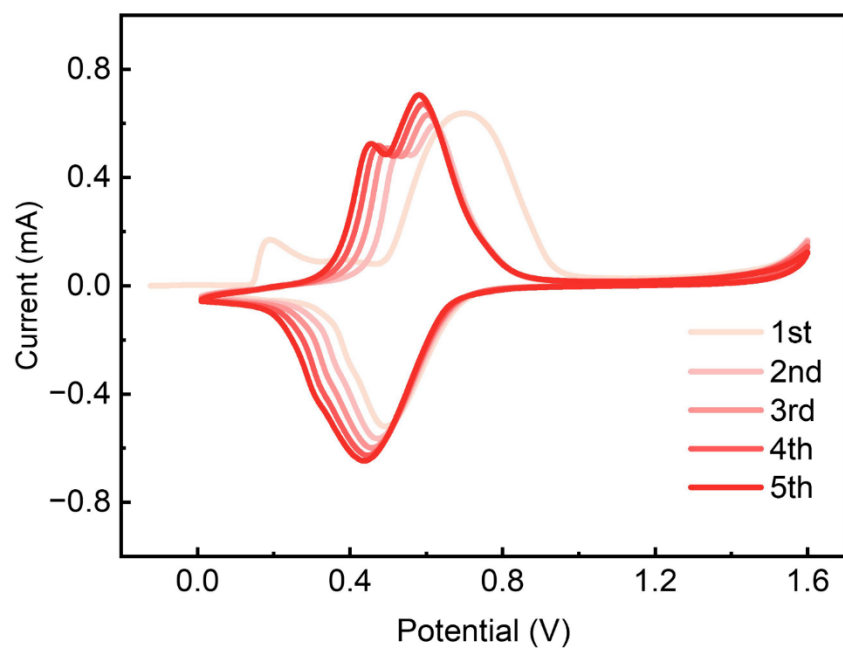
Supplementary Figure 13. XRD patterns of anode material MoO_3 .



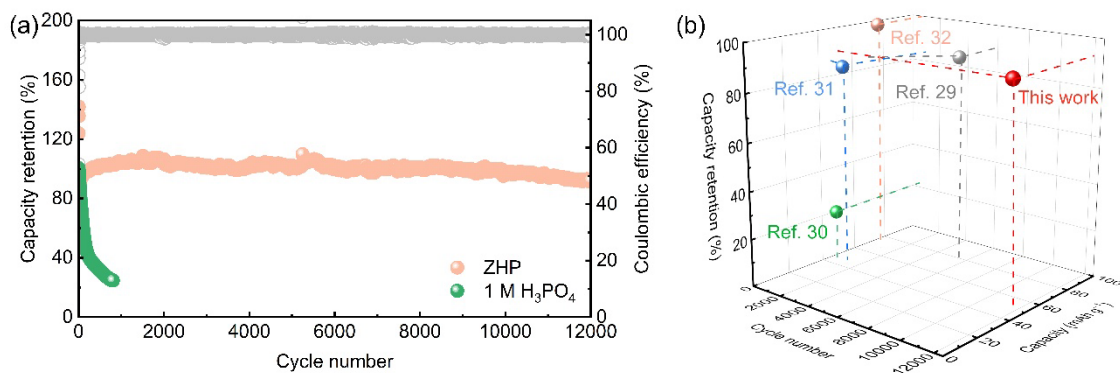
Supplementary Figure 14. a-c) SEM images of H-TBA and MoO₃, and its corresponding elementals mapping of Fe (b1), Cu (b2) and Mo.



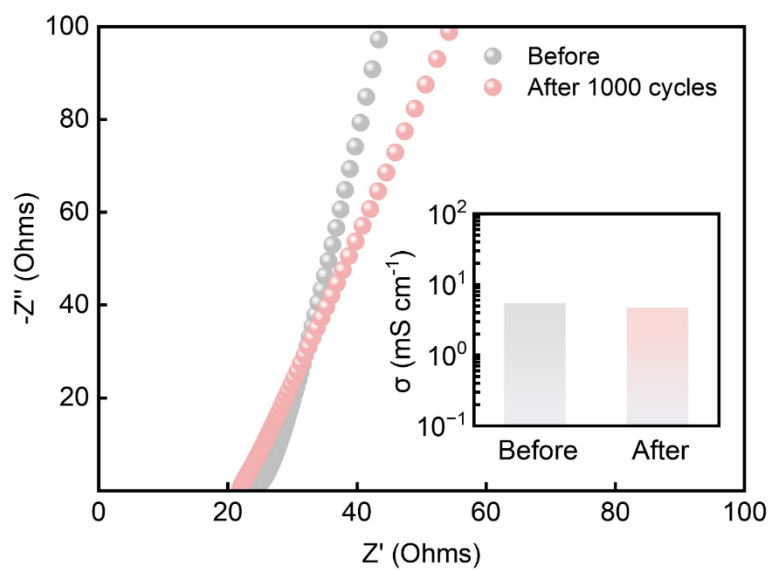
Supplementary Figure 15. Galvanostatic charge/discharge profiles for full battery at various temperatures.



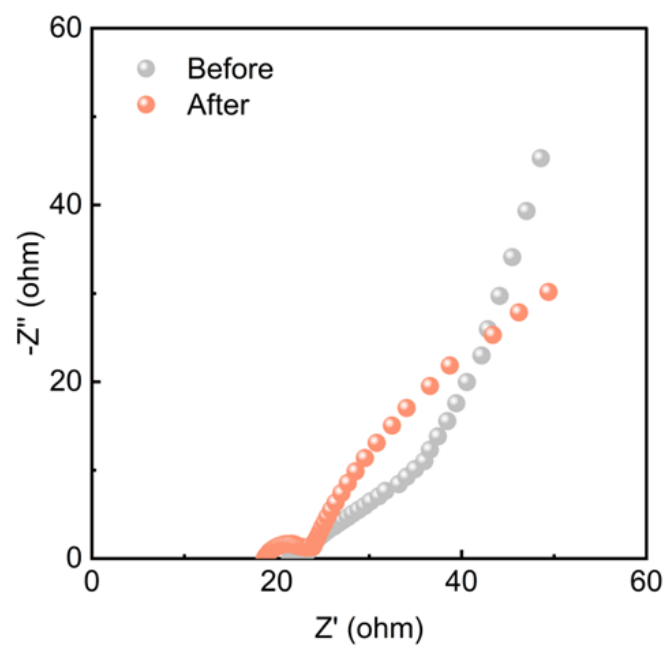
Supplementary Figure 16. Cyclic voltammetry curves of H-TBA/ZHP/MoO₃ full cell at 1 mV s⁻¹.



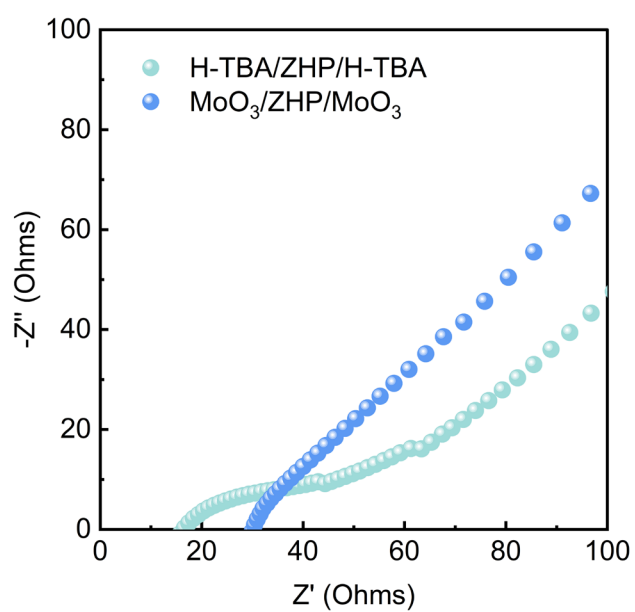
Supplementary Figure 17. (a) Long-cycle performance of H-TBA//MoO₃ full cells in different electrolytes at a current density of 1000 mAh·g⁻¹. (Note: The grey colour corresponds to the coulombic efficiency of H-TBA/ZHP/MoO₃.) (b) Performance comparison between full cells with ZHP electrolyte and aqueous H₃PO₄ electrolyte. (See Table S7 for details.)



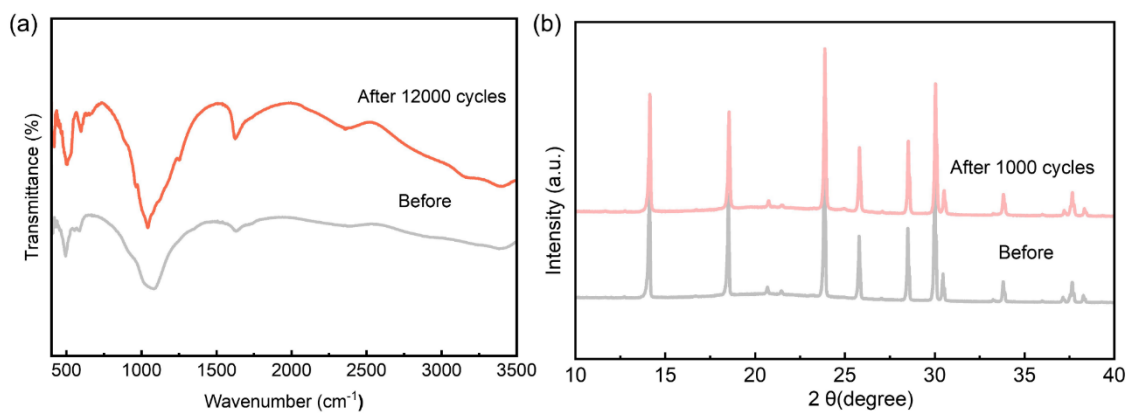
Supplementary Figure 18. Nyquist plots of ZHP before used and after 1000 cycles under dry condition ($\text{RH} \ll 1\%$) at room temperatures. The inset diagram shows the ionic conductivity of ZHP before and after 1000 cycles.



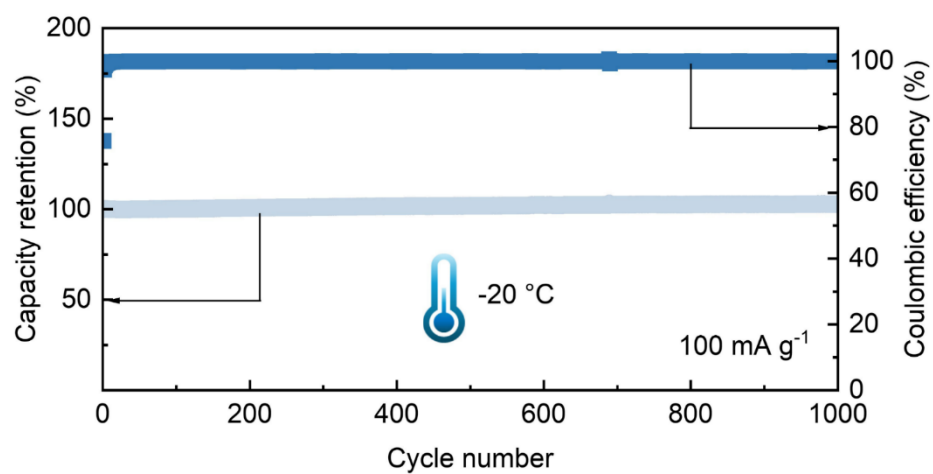
Supplementary Figure 19. Nyquist plots of the full cell before and after cycling.



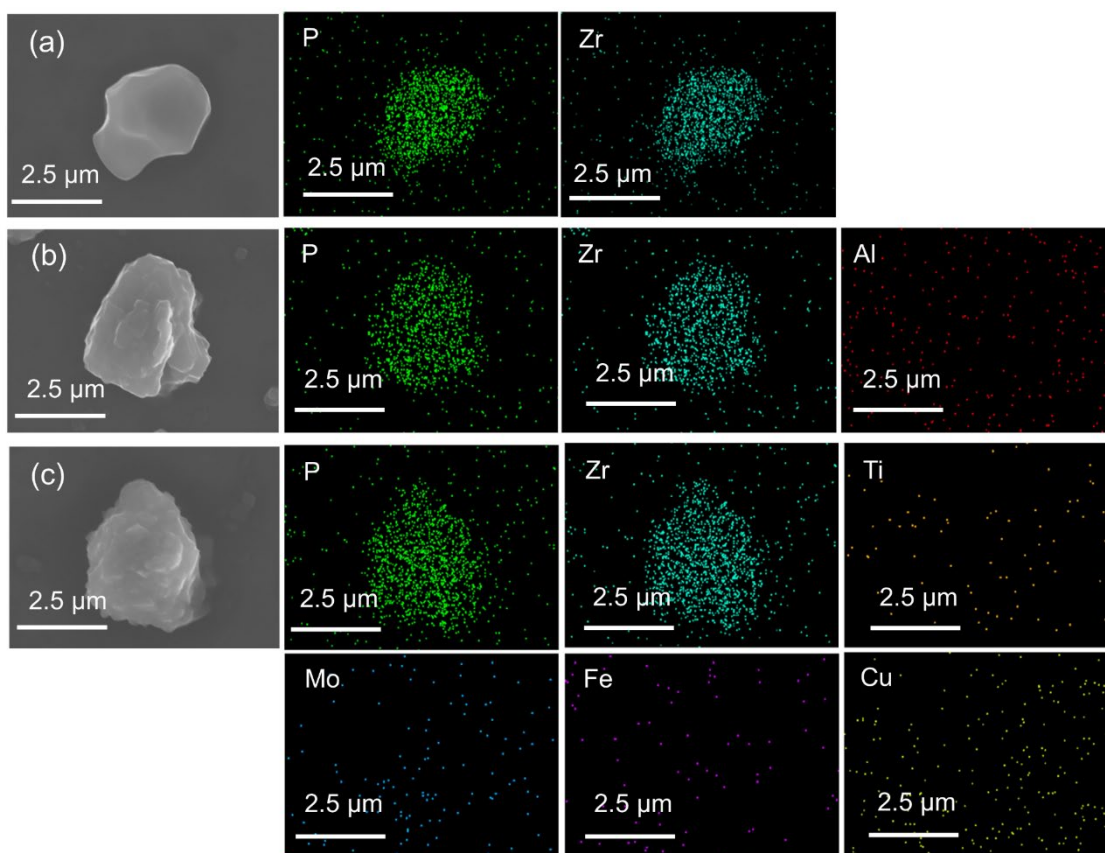
Supplementary Figure 20. Nyquist spectra of H-TBA/ZHP/H-TBA and MoO₃/ZHP/MoO₃ symmetric cells at room temperature.



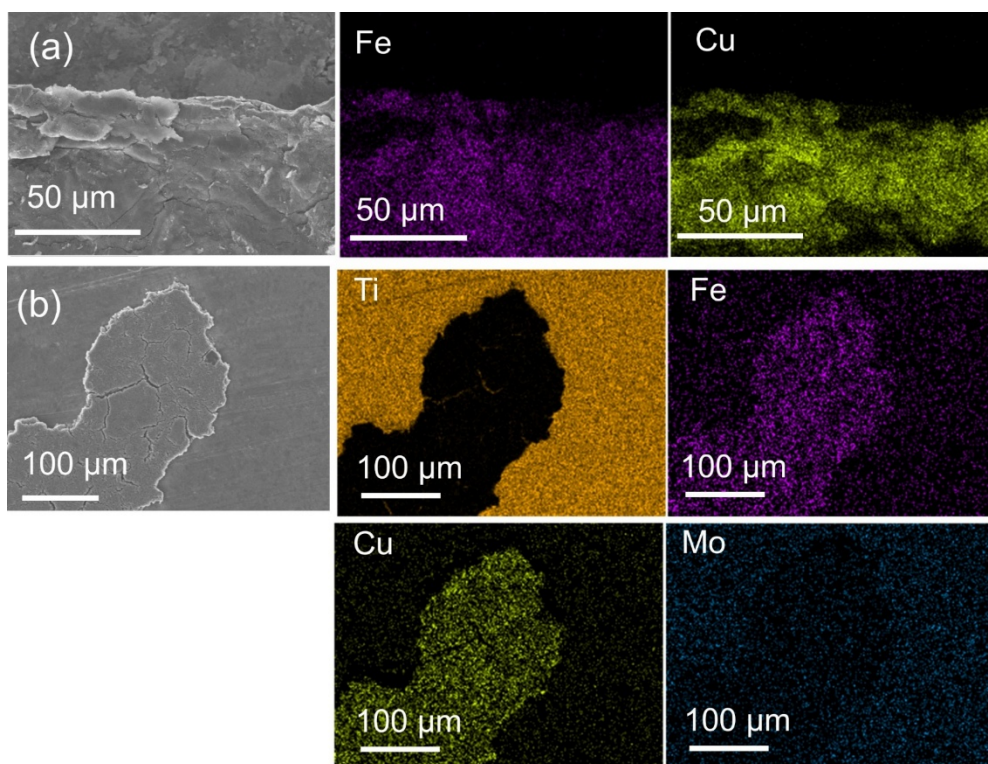
Supplementary Figure 21. a) FT-IR curves of ZHP before used and after 12000 cycles. b) XRD patterns for ZHP before used and after 1000 cycles.



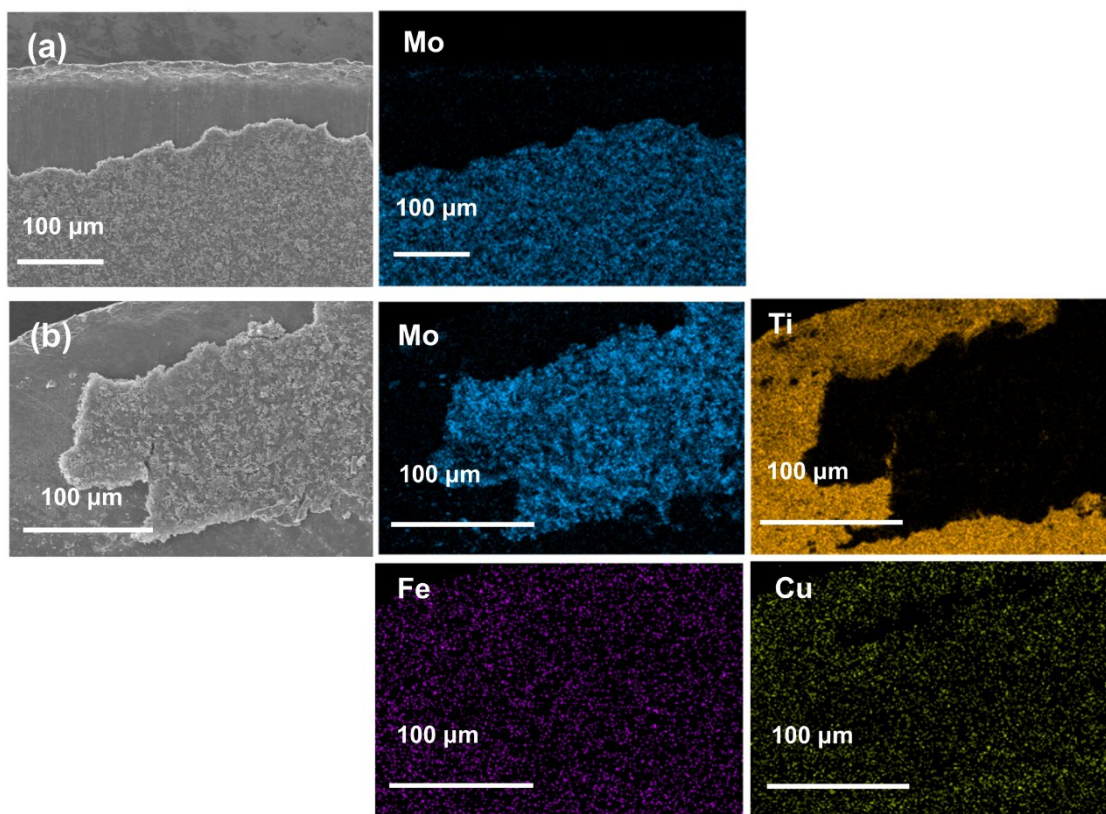
Supplementary Figure 22. Cyclability and coulombic efficiency of all solid-state proton cell at current densities 100 mA g⁻¹ at -20 °C.



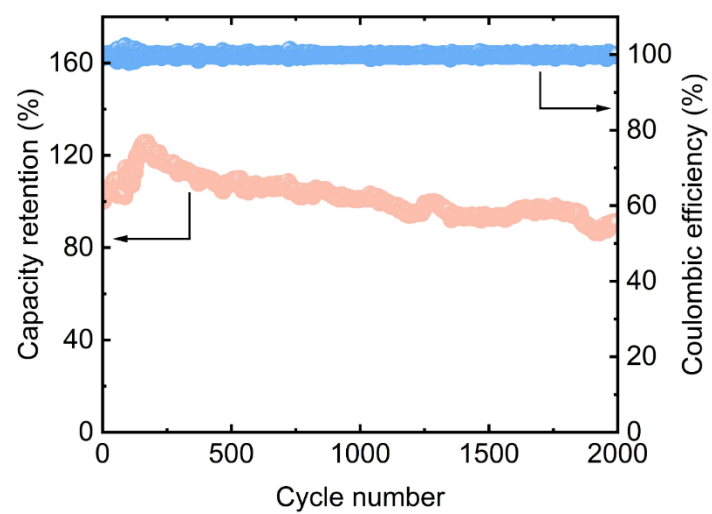
Supplementary Figure 23. a) SEM images of initial ZHP powder and its corresponding elementals mapping of P and Zr. b) SEM images of ZHP, which were assembled with Al foils for 10 days. And its corresponding elementals mapping of P, Zr and Al. c) SEM images of after 12000 cycles of ZHP electrolyte and its corresponding elementals mapping of P, Zr, Ti, Cu, Fe and Mo.



Supplementary Figure 24. a) SEM images of initial H-TBA electrode and its corresponding elementals mapping of Cu and Fe. b) SEM images of after 12000 cycles of H-TBA electrode and its corresponding elementals mapping of Ti, Cu, Fe and Mo.



Supplementary Figure 25. a) SEM images of initial MoO₃ electrode and its corresponding elementals mapping of Cu and Fe. b) SEM images of after 12000 cycles of MoO₃ electrode and its corresponding elementals mapping of Ti, Cu, Fe and Mo.



Supplementary Figure 26. Long cycles of the full-cell H-TBA/ZHP/MoO₃ with Al foil as the current collector at a current density of 1000 mA g⁻¹.

REFERENCES

- [1] Steiner, T. The Hydrogen Bond in the Solid State. *Angew. Chem. Int. Ed.* **2002**, *41* (1), 48-76.
DOI: 10.1002/1521-3773(20020104)41:1<48::AID-ANIE48>3.0.CO;2-U.
- [2] Yan, L.; Huang, J.; Guo, Z.; et al. Solid-State Proton Battery Operated at Ultralow Temperature. *ACS Energy Lett.* **2020**, *5* (2), 685-691. DOI: 10.1021/acsenenergylett.0c00109.
- [3] Sun, W.; Xu, Z.; Qiao, C.; et al. Antifreezing Proton Zwitterionic Hydrogel Electrolyte via Ionic Hopping and Grotthuss Transport Mechanism toward Solid Supercapacitor Working at -50 °C. *Adv. Sci.* **2022**, *9* (27), 2201679. DOI: 10.1002/advs.202201679.
- [4] Gui, D.; Zhang, Y.; Li, H.; et al. Developing a Unique Hydrogen-Bond Network in a Uranyl Coordination Framework for Fuel Cell Applications. *Inorg. Chem.* **2022**, *61* (20), 8036-8042. DOI: 10.1021/acs.inorgchem.2c00844.
- [5] Wang, L.-L.; Ni, X.-Q.; Han, Y.-J.; et al. cidified Naphthalene Diimide Covalent Organic Frameworks with Superior Proton Conduction for Solid-State Proton Batteries. *J. Mater. Chem. C* **2025**, 10.1039/D4TC04322G. DOI: 10.1039/D4TC04322G.
- [6] Qin, Z.; Li, X.; Dong, Q.; et al. Limiting Interfacial Free Water and Proton Concentration by Hydrogel Electrolytes for Stable MoO₃ Anode in a Proton Battery. *Small* **2024**, *20* (32), 2400108. DOI: 10.1002/sml.202400108.
- [7] Wang, S.; Jiang, H.; Dong, Y.; et al. Acid-in-Clay Electrolyte for Wide-Temperature-Range and Long-Cycle Proton Batteries. *Adv. Mater.* **2022**, *34* (23), 2202063. DOI: 10.1002/adma.202202063.
- [8] Meng, F.; Dong, X.; Wu, H.; et al. Crystalline Hydrogen Enhanced Dual-Acid Quasi-Solid-State Proton Battery. *Adv. Funct. Mater.* **2025**, *35* (23). DOI: 10.1002/adfm.202422079.
- [9] Xu, Y.; Wu, X.; Jiang, H.; et al. A Non-Aqueous H₃PO₄ Electrolyte Enables Stable Cycling of Proton Electrodes. *Angew. Chem. Int. Ed.* **2020**, *59* (49), 22007-22011. DOI: 10.1002/anie.202010554.
- [10] Li, H.-Y.; Liu, Y.-L. Nafion-Functionalized Electrospun Poly(Vinylidene Fluoride) Nanofibers for High-Performance Proton Exchange Membranes in Fuel Cells. *J. Mater. Chem. A* **2014**, *2* (11), 3783-3793. DOI: 10.1039/C3TA14264G.
- [11] Xie, Z.; Wu, H.; Wu, Q.; et al. Synthesis and Performance of Solid Proton Conductor

- Molybdovanadosilicic Acid. *RSC Adv.* **2018**, 8 (25), 13984-13988. DOI: 10.1039/C8RA02390E.
- [12] Zhao, F. J.; Zhu, Y.; Chen, Y.; et al. Acidified Nitrogen Self-Doped Porous Carbon with Superprotonic Conduction for Applications in Solid-State Proton Battery. *Small* **2024**, 20 (8), e2305765. DOI: 10.1002/smll.202305765.
- [13] Fop, S.; Vivani, R.; Masci, S.; et al. Anhydrous Superprotonic Conductivity in the Zirconium Acid Triphosphate $\text{ZrH}_5(\text{PO}_4)_3$. *Angew. Chem. Int. Ed.* **2023**, 62 (18), e202218421. DOI: 10.1002/anie.202218421.
- [14] Ren, X.-Y.; Song, J.-B.; Zhang, G.-Q.; et al. Covalent Organic Framework with Superior Proton Conduction for Solid-State Proton Battery Application. *ACS Mater. Lett.* **2024**, 6 (9), 4036-4041. DOI: 10.1021/acsmaterialslett.4c01140.
- [15] Liu, S. T.; Ma, X. R.; Zhao, F. J.; et al. Solid-State Proton Battery With Record High Specific Capacity Enabled by Covalent-Organic Framework Electrolyte. *Adv. Funct. Mater.* **2025**. DOI: 10.1002/adfm.202507054.
- [16] Zhang, G. Q.; Liu, B.; Li, H. Y.; et al. Acidification of Polyphthalocyanine Boosts Solid-State Proton Battery Performance with High Specific Capacity and Robust Cycling Stability. *Small* **2025**, e2505839. DOI: 10.1002/smll.202505839.
- [17] Ma, N.; Kosasang, S.; Yoshida, A.; et al. Proton-Conductive Coordination Polymer Glass for Solid-State Anhydrous Proton Batteries. *Chem. Sci.* **2021**, 12 (16), 5818-5824. DOI: 10.1039/D1SC00392E.
- [18] Dong, X.; Li, Z.; Luo, D.; et al. Pre-Protonated Vanadium Hexacyanoferrate for High Energy-Power and Anti-Freezing Proton Batteries. *Adv. Funct. Mater.* **2023**, 33 (11), 2210473. DOI: 10.1002/adfm.202210473.
- [19] Jiang, H.; Shin, W.; Ma, L.; et al. A High-Rate Aqueous Proton Battery Delivering Power Below $-78\text{ }^\circ\text{C}$ via an Unfrozen Phosphoric Acid. *Adv Energy Mater* **2020**, 10 (28), 2000968. DOI: 10.1002/aenm.202000968.
- [20] Cui, Z.; Wang, D.; Xu, T.; et al. Enabling Extreme Low-Temperature Proton Pseudocapacitor with Tailored Pseudocapacitive Electrodes and Antifreezing Electrolyte Engineering. *Chem. Eng. J.* **2024**, 495, 153347. DOI: 10.1016/j.cej.2024.153347.

- [21] Kreuer, K.-D. Proton Conductivity: Materials and Applications. *Chem. Mater.* **1996**, 8 (3), 610-641. DOI: 10.1021/cm950192a.
- [22] Golubev, N. S.; Asfin, R. E.; Smirnov, S. N.; et al. Study of Hydrogen Bonds of Hypophosphorous Acid by ^1H , ^2H , ^{31}P , and ^{15}N NMR Spectroscopy under Slow Exchange Conditions. *Russ. J. Gen. Chem.* **2006**, 76 (6), 915-924. DOI: 10.1134/S1070363206060119.
- [23] Reeves, L. W.; Schneider, W. G. Nuclear Magnetic Resonance Studies of Hydrogen Bonding in Acetic Acid. *Trans. Faraday Soc.* **1958**, 54, 314-320. DOI: 10.1039/TF9585400314.
- [24] Nibbering, E. T. J.; Elsaesser, T. Ultrafast Vibrational Dynamics of Hydrogen Bonds in the Condensed Phase. *Chem. Rev.* **2004**, 104 (4), 1887-1914. DOI: 10.1021/cr020694p.
- [25] Joshi, V. S.; Joshi, M. J. FTIR Spectroscopic, Thermal and Growth Morphological Studies of Calcium Hydrogen Phosphate Dihydrate Crystals. *Cryst. Res. Technol.* **2003**, 38 (9), 817-821. DOI: 10.1002/crat.200310100.